


Article

Removal of NO_x Using Hydrogen Peroxide Vapor over Fe/TiO₂ Catalysts and an Absorption Technique

Lei Chen ¹, Yuxin Li ¹, Qinxin Zhao ^{1,*}, Yungang Wang ¹, Zhiyuan Liang ¹ and Qiang Lu ² 

¹ Key Laboratory of Thermo-Fluid Science and Engineering of MOE, School of Energy and Power Engineering, Xi'an Jiaotong University, Xi'an 710049, China; chenlei7166@163.com (L.C.); happyalex1986@163.com (Y.L.); ygwang1986@xjtu.edu.cn (Y.W.); liangzy@xjtu.edu.cn (Z.L.)

² National Engineering Laboratory for Biomass Power Generation Equipment, North China Electric Power University, Beijing 102206, China; qianglu@mail.ustc.edu.cn

* Correspondence: zhaoqx@mail.xjtu.edu.cn

Received: 17 October 2017; Accepted: 5 December 2017; Published: 13 December 2017

Abstract: In this study, we proposed an innovative oxidation–absorption method for low-temperature denitrification (160–240 °C), in which NO is initially catalytically oxidized by hydrogen peroxide (H₂O₂) vapor over titania-based catalysts, and the oxidation products are then absorbed by NaOH solution. The effects of flue gas temperature, molar H₂O₂/NO ratio, gas hourly space velocity (GHSV), and Fe substitution amounts of Fe/TiO₂ catalysts on the denitrification efficiency were investigated by a well-designed experiment. The results indicated that the Fe/TiO₂ catalyst exhibited a combination of remarkable activity and deep oxidation ability (NO converted into harmless NO₃[−]). In order to comprehend the functional mechanism of the Fe dopant's local environment in TiO₂ support, the promotional effect of the calcination temperature of Fe/TiO₂ on the denitration performance was also studied. A tentative synergetic mechanism could be interpreted from two aspects: (1) Fe³⁺ as a substitute of Ti⁴⁺, leading to the formation of enriched oxygen vacancies at the surface, could significantly improve the adsorption efficiency of •OH; (2) the isolated surface Fe ion holds a strong adsorption affinity for NO, such that the adsorbed NO could be easily oxidized by the pre-formed •OH. This process offers a promising alternative for current denitrification technology.

Keywords: oxidation–absorption; H₂O₂; NO_x; catalytic oxidation; TiO₂ substrate

1. Introduction

Increasingly serious environmental pollution has brought with it a significant threat to human survival and the ecological system, wherein the discharge of atmospheric pollutants, which mainly include nitric oxide (NO_x), has become the main phenomenon responsible for acid deposition, photochemical smog, and respiratory disease in mankind.

Conventional strategies for NO_x control are mainly categorized into three groups: pre-combustion, combustion modification, and post-combustion technologies [1]. Since pre-combustion and combustion modification could not meet the strict new emissions regulations, they are often adopted as an adjunctive way to control NO_x. The post-combustion technologies, which mainly include the selective catalytic reduction method (SCR), the selective non-catalytic reduction method (SNCR), electron-beam, and absorption, are the primary methods for NO_x elimination. As the most common way to control NO_x, SCR is capable of achieving a high level of NO_x removal efficiency: up to 85% [2]. Nevertheless, this process suffers from problems, such as a high and narrow operating temperature window (300–400 °C), NH₃ slip, and the poisoning of the catalyst [3]. Other deNO_x methods suffer from the defects of requiring a high amount of investment capital or having a low efficiency. Therefore, a cost-effective and environmentally friendly strategy for reducing NO_x was overpoweringly needed. Fortunately, advanced oxidation technology seems to be a promising

approach and has drawn much attention recently. The ultraviolet (UV)/H₂O₂ advanced oxidation process is a typical method for purifying flue gas and can achieve a relatively high NO oxidation efficiency [4,5]. However, this breakthrough technique was found to be hard to realize for a real scale application due to a high operating cost and unfeasibility for implementation. The catalytic decomposition of gas-phase H₂O₂ into •OH seemed to be an appealing alternative due to its mild reaction conditions and environment-friendly advantage. Ding and his colleague had attempted to produce a series of iron-based catalysts for the catalytic decomposition of H₂O₂ and achieved an ~80% NO_x removal efficiency [6–8]. Nonetheless, the method is stoichiometrically limited by hydrogen peroxide (H₂O₂/NO molar ratio = 450~800:1), and consequently it is difficult to use for widespread application. Recently, Zhao et al. adopted nanoscale zerovalent iron to activate vaporized H₂O₂ for removing NO, and the NO removal efficiency was 80.4% at the price of a low H₂O₂ dosage (H₂O₂/NO molar ratio = 10~30:1) [9]. Moreover, Wu further decreased the H₂O₂/NO molar ratio to 4~16:1 by employing the solid-phase Fe₂(SO₄)₃ and La_{1-x}Ca_xFeO₃ oxides as the catalysts [10,11]. However, they focused more attention on the removal efficiency of NO, irrespective of the potential intermediates and their individual hazards. In this regard, the undesired intermediate products (NO₂ and NO₂⁻), which are recognized to be more detrimental than NO, were usually ignored as DeNO_x indexes to evaluate the performance of NO_x abatement.

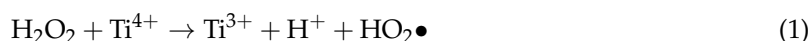
TiO₂ is considered to be an ideal catalyst for the removal of air pollutants—including NO_x—due to its excellent chemical stability, low cost, and nontoxicity toward both humans and the environment [12]. Recent studies have proven that H₂O₂ can act both as an oxidant and as a reductant via a redox path of Ti³⁺/Ti⁴⁺ when the decomposition reaction of a H₂O₂ molecule over a TiO₂ surface occurs [13]. It should be noted that defective surface sites, especially for the oxygen vacancies, play a significant role in the decomposition of H₂O₂ [14]. However, the limited quantity of oxygen vacancies on a pure TiO₂ surface retards its capacity for the generation of •OH by activating H₂O₂. The doping of hetero-valence ions in the host lattice seems to be a good choice to resolve this problem.

In this paper, a series of Fe/TiO₂ catalysts has been synthesized by a conventional co-precipitation method and applied in the catalytic decomposition of H₂O₂ for treating NO_x. The possible intermediate products and their individual hazards in the nitric oxide oxidation process were comprehensively considered to evaluate the catalytic performance of the catalysts. Remarkably, the prepared material achieved a combination of high NO_x removal efficiency and deep oxidation ability.

2. Results and Discussion

2.1. Effects of Molar H₂O₂/NO and Temperature

The effect of molar H₂O₂/NO with temperature on denitration was studied experimentally as shown in Figure 1a–c. Blank tests were also performed using various H₂O₂ solutions without catalyst (Figure S1). The tests showed that at 160–240 °C the highest NO_x removal efficiency under different H₂O₂/NO ratios was less than 25%. The significant increase of NO oxidation efficiency in the presence of catalyst could be attributed to the activated species produced from catalytic decomposition of H₂O₂ vapor. The catalytic mechanism of a H₂O₂ molecule over TiO₂ is analogous to the Fenton-type mechanism, and the reaction pathways can be described by the following equations [13,15]:



As observed in Figure 1a, for the molar H₂O₂/NO range from 8 to 24, the NO oxidation efficiency displayed an increasing and then a decreasing tendency with an increase in reaction temperature. The optimum NO oxidation efficiency reached at 200 °C. In contrast, the NO oxidation values for the molar H₂O₂/NO of 48 varied slightly with temperature and maintained a higher level than the others. NO₂ selectivity (Figure 1b) was positively associated with the temperature, and the growth of

NO₂ at a high-temperature segment could be due to the decomposition of formed nitrates [16]. As a consequence, the total amount of NO_x removal (Figure 1c) for the molar H₂O₂/NO range from 8 to 24 achieved a highest value at 200 °C, and showed a moderating trend along with the temperature for the molar H₂O₂/NO of 48. It is worth noting that the efficiency values of NO oxidation increased with an increase in the molar H₂O₂/NO, while the NO₂ selectivity firstly increased as the molar H₂O₂/NO rose from 8 to 24 and then declined with a further increase of molar H₂O₂/NO. This phenomenon could be interpreted in two respects: (1) the increase of molar H₂O₂/NO implied that more H₂O₂ molecules participated in the reaction with NO; however, the weak oxidative capacity of H₂O₂ molecules could not implement a completed oxidation process of NO [17,18]; and (2) the weakening of the concentration effect for the molar H₂O₂/NO of 48 was mainly ascribed to the quenching of •OH; i.e., •OH radicals were depleted in the side-reaction and H₂O₂ was also a radical scavenger in addition to the source of •OH (Equations (3)–(6)) [19,20]. Meanwhile, the molar percentage of NO₃[−] increased from 36.8% to 62.1% as the molar H₂O₂/NO rose from 8 to 24, and then dropped to 58.7% with a further increase of molar H₂O₂/NO (Figure 1d). This trend strengthened the abovementioned analysis.

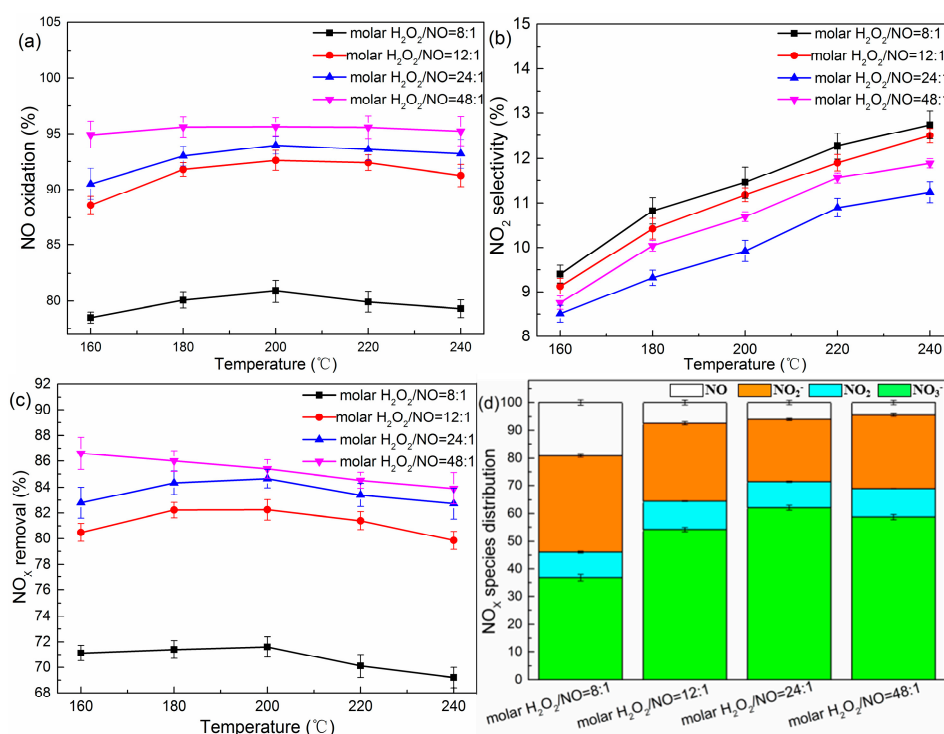


Figure 1. (a–d) Removal efficiencies of nitric oxide (NO_x) under different reaction systems. Conditions: H₂O₂/NO molar ratio: 8:1, 12:1, 24:1, and 48:1; catalyst: TiO₂ (P25, Evonik Industries AG); gas hourly space velocity (GHSV) = 60,000 h^{−1}.

2.2. Effects of the Gas Hourly Space Velocity (GHSV)

A series of experiments with different GHSV were conducted. As shown in Figure 2a–c, the performance of denitration strongly depended on the space velocity. A higher GHSV (>60,000 h^{−1})

displayed a NO_x removal efficiency of more than 80% in the temperature range from 160 °C to 240 °C. As demonstrated by Li et al. [21], H_2O_2 could easily be adsorbed by the TiO_2 surface and give rise to surface complexes, and further be converted into $\bullet\text{OH}$, which is highly reactive and interacts with NO rapidly. Theoretically, the NO_x removal efficiency should increase with a decline of GHSV from $60,000\text{ h}^{-1}$ to $30,000\text{ h}^{-1}$. However, the observed results showed a contrary tendency. This phenomenon could be interpreted such that the surface nitrate would decompose into NO_2 on the TiO_2 surface when the catalyst dosage was excessive [22]. In the meanwhile, the Ti^{3+} species generated in the redox process might have reacted with NO_2 (Equation (7)), thus facilitating the generation of NO [10,23].

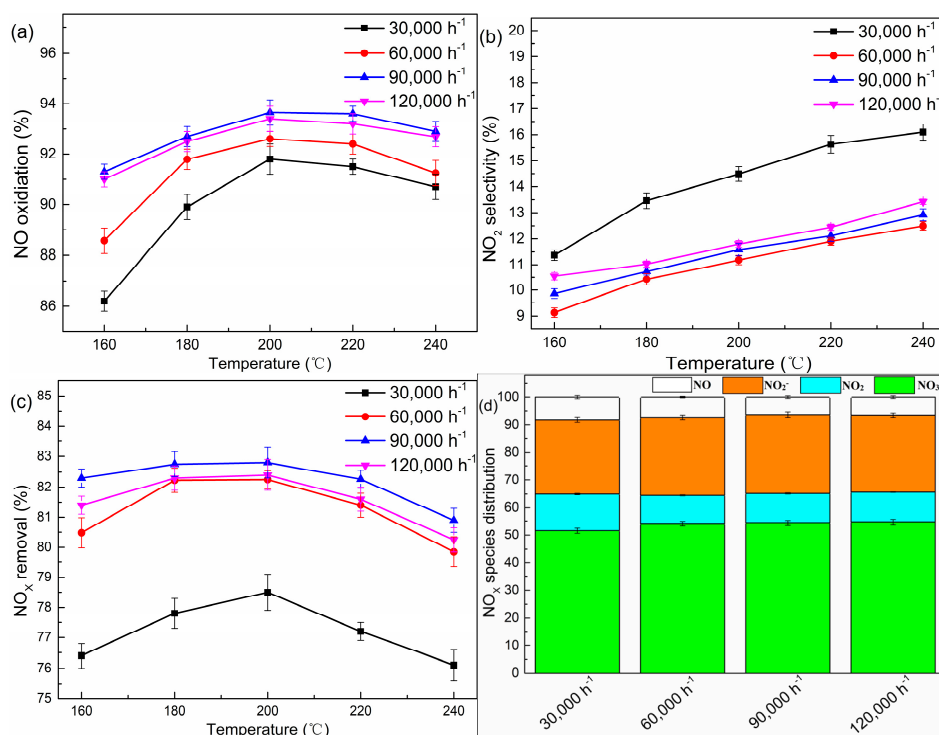


Figure 2. (a–d) Removal efficiencies of NO_x under different GHSV. Conditions: $\text{H}_2\text{O}_2/\text{NO}$ molar ratio: 12:1; catalyst: P25.

2.3. Effects of Catalyst Type

To investigate the effect of TiO_2 from different sources and Fe substitution amounts on the removal efficiency of NO_x , a series of experiments with different catalyst types were performed. As depicted in Figure 3a–c, TiO_2 exhibited a higher NO oxidation efficiency compared with P25, while both gave a $\sim 10\%$ NO_2 selectivity. With the introduction of an iron ion, the NO oxidation efficiency increased slightly while NO_2 selectivity declined at the same time. This trend led to a significant increase in the total NO_x removal efficiency, especially for the 2% Fe- TiO_2 , which was up to 94%. We also selected the nitrogen species distribution at 200 °C to further confirm the positive effect of the iron ion. As illustrated in Figure 3d, the molar percentage of NO_3^- increased from 78.7% to 88.1% when the iron molar concentration increased from 0.5% to 2% and then dropped by 1.8% with a 3% Fe- TiO_2 . Moreover, the percentage of NO_2^- was significantly less than TiO_2 without an iron ion. This strengthened the fact that the iron ion facilitated the deep oxidation ability which turned NO into NO_3^- .

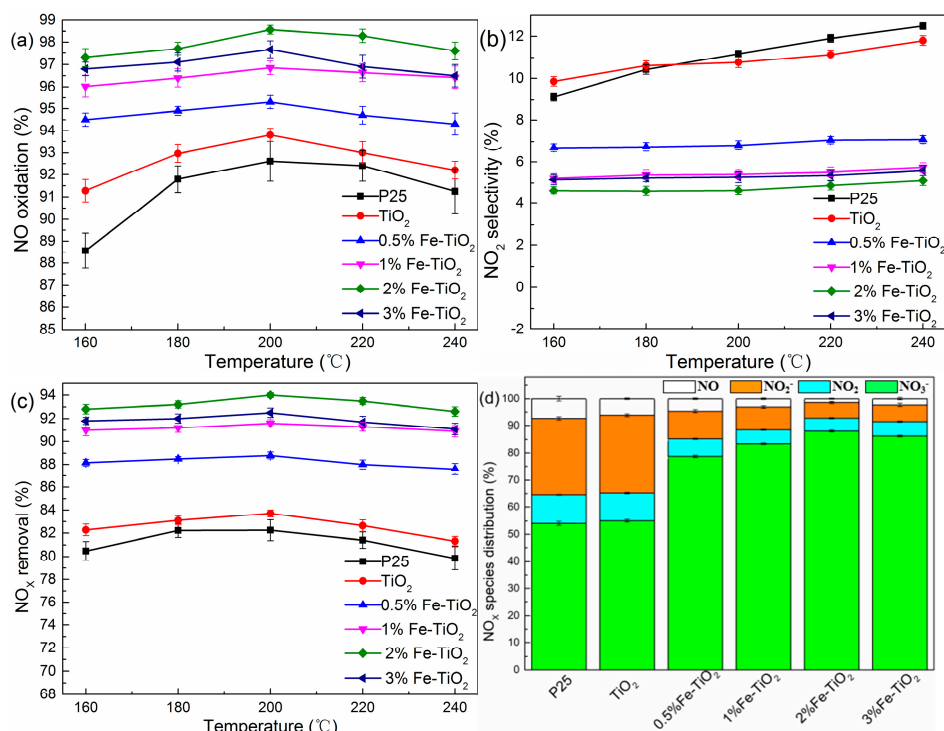


Figure 3. (a–d) Removal efficiencies of NO_x under different catalyst types. Conditions: H₂O₂/NO molar ratio: 12:1; GHSV: 60,000 h⁻¹.

2.4. Structural Properties of Catalyst

Figure 4 displays the Raman scattering spectra of the tested catalysts. The P25 and iron-doped titanium dioxides with different molar ratios (0%, 0.5%, 1%, 2%, and 3%) showed similar spectral characteristics. The observed peaks at 144 cm⁻¹, 195 cm⁻¹, 395 cm⁻¹, 515 cm⁻¹, and 638 cm⁻¹ belong to the Raman active of TiO₂ with symmetries of E_g(1), E_g(2), B_{1g}(1), B_{1g}(2), and E_g(3), respectively [24,25]. It should be mentioned that no Fe-relevant structures could be observed in the sample obtained above 400 °C, confirming that the Fe atom may substitute for the Ti atom and be highly dispersed in the lattice of TiO₂.

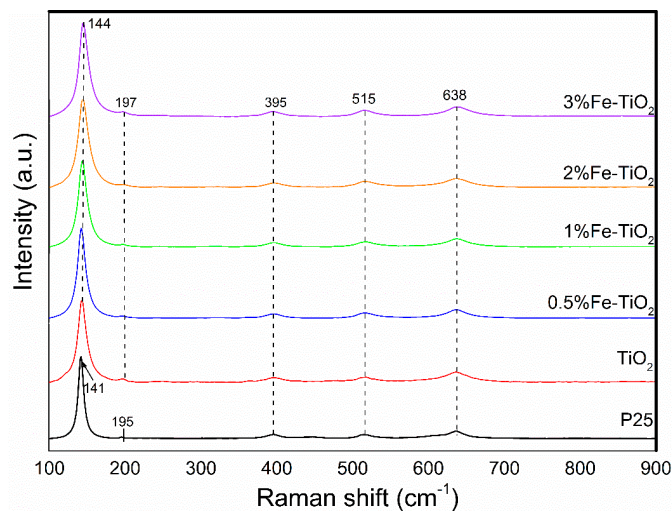


Figure 4. Raman spectra of pure and iron oxide-supported TiO₂ catalyst.

The N₂ adsorption–desorption isotherms of the samples and the Brunauer–Emmett–Teller (BET) value are presented in Figure S2 and Table 1. From Figure S2, all of the samples showed a typical IV-type pattern according to the Brunauer–Deming–Deming–Teller (BDDT) classification. The 3% Fe-TiO₂ displayed hysteresis loops in the relative pressure of 0.4–0.8, which represented mesoporous materials (2–50 nm). Nevertheless, the other samples exhibited two capillary condensation steps, suggesting bimodal pore size distributions in the mesoporous and microporous regions [26]. The BET specific surface area of the P25 and pure TiO₂ was 36.7 and 98.6 m²·g^{−1}, respectively. It should be mentioned that a sharp decrease in surface area was observed when the doping content exceeded 1 mol %, which was possibly due to a solubility limit for Fe³⁺ ions in the crystal structure of anatase and the excess Fe³⁺ ion blocking the pore channel of TiO₂ [27].

Table 1. Textural properties of the samples.

Catalyst	Surface Area (m ² ·g ^{−1})	Crystallite Size (nm)	Pore Volume (cm ³ ·g ^{−1})	Pore Radius (Å)
P25	36.7	26.23	0.087	106.1
TiO ₂	98.6	11.16	0.162	41.3
0.5% Fe-TiO ₂	80.4	12.96	0.226	48.9
1% Fe-TiO ₂	92.3	11.75	0.213	42.8
2% Fe-TiO ₂	66.9	11.27	0.157	44.3
3% Fe-TiO ₂	66.4	10.62	0.079	25.8

The XRD patterns of the tested catalysts are depicted in Figure 5. The P25 revealed a pattern characteristic of both a rutile and anatase phase, while the crystal structures of the doped and undoped samples prepared by the co-precipitation method were all anatase (JCPDS S#21-1272). For the diffraction patterns of the Fe-doped TiO₂ samples, all diffraction peaks were congruent with TiO₂ and no peaks attributable to iron species could be observed in the investigated range. The possible reason was that the Fe atoms had successfully replaced Ti atoms and were incorporated into the crystal framework of the TiO₂ lattice due to a similar ionic radius of Fe³⁺ (0.69 Å) and Ti⁴⁺ (0.745 Å) [28,29]. As presented in Table 1, iron species loading also impacted on the crystallite size of the samples significantly. The maximum crystallite size was found in the material with dopant concentrations of around 0.5 mol %. This phenomenon was in good agreement with the attainment, which suggested a solubility limit for Fe³⁺ ions in the anatase structure owing to lattice expansion that arises from compensating effects between the Fe³⁺ substitution of Ti⁴⁺ and oxygen vacancy formation for the maintenance of charge neutrality [30,31].

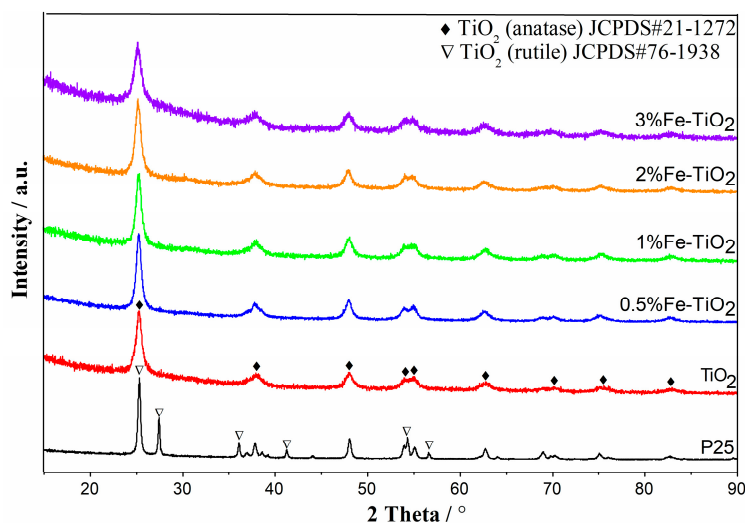


Figure 5. XRD results of the tested catalysts.

FE-SEM micrographs of undoped and doped TiO_2 nanoparticles are shown in Figure S3. The average particle size of the P25 sample was significantly larger than the catalysts prepared by the co-precipitation method, and all samples revealed a fine and uniform spherical particulate structure. The morphology structures of the samples were characterized by TEM (transmission electron microscopy) and HRTEM (high resolution transmission electron microscopy). As shown in Figure 6a–d, a uniform isolated individual particle can be observed in the Fe-doped TiO_2 samples. The HRTEM image of all of the Fe- TiO_2 samples indicates that the obtained TiO_2 particles were mainly in the anatase phase (Figure 6e,f), wherein a well-ordered lattice fringe spacing of 0.35 nm corresponded to the (1 0 1) crystallographic plane of anatase, and the results were consistent with the XRD analysis [32]. It can be easily observed in the EDX (energy-dispersive X-ray spectrometry) mapping of the 2% Fe- TiO_2 that the iron element was homogeneously dispersed onto the TiO_2 support (Figure 6g–j), and this finding clearly raised the conclusion that the present preparation method provided a well-dispersed metal loading over the supported sample.

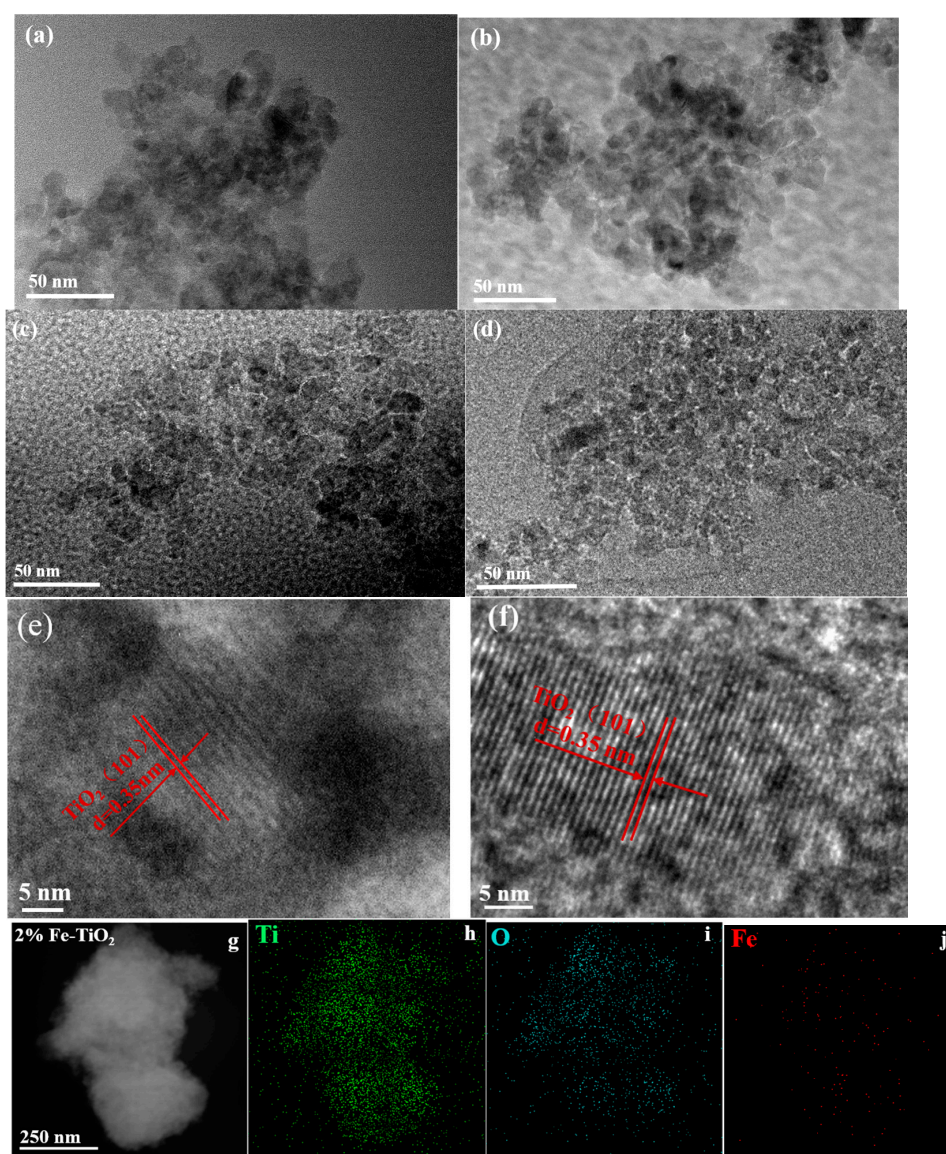


Figure 6. TEM and HRTEM results of the dopant Fe- TiO_2 serial catalysts: (a) 0.5% Fe- TiO_2 (b) 1% Fe- TiO_2 (c) 2% Fe- TiO_2 (d) 3% Fe- TiO_2 (e) of 1% Fe- TiO_2 sample (f) of 3% Fe- TiO_2 sample (g–j) EDX mapping analyses for 2% Fe- TiO_2 .

In addition, XPS measurements were conducted to further ascertain the chemical status of the surface of the Fe-doped TiO₂ nanoparticles. The corresponding results are presented in Figure 7. As shown in Figure 7a, the fully scanned spectra demonstrated the existence of Ti, O, and Fe elements, as well as C as the reference (C 1s calibrated with a fixed value of 284.8 eV). According to the core level spectra of Fe 2p (given in Figure 7a as inset), the presence of Fe 2p_{3/2} and Fe 2p_{1/2} components in the 0.5% Fe-TiO₂ and 1% Fe-TiO₂ samples at the binding energy (B.E.) positions of 710.9 eV and 724.3 eV were consistent with Fe³⁺ in an interactive Ti-O-Fe species [33]. A higher shift of the binding energies of Fe 2p_{3/2} and Fe 2p_{1/2} could be observed with a further increase in Fe concentration, and this phenomenon was caused by the existence of the adsorbed Fe³⁺ dopant on the surface of the TiO₂ [34]. The existence of Fe³⁺ on the TiO₂ surface was likely to increase the number of available adsorption sites and lower the surface desorption energy [34,35]. A slight shift was also observed in the presence of Ti 2p_{3/2} and Ti 2p_{1/2} when the Fe-doped concentration exceeded 2 mol %, and all peaks regarding Ti 2p indicated that the Ti elements in the samples were in agreement with the values of Ti⁴⁺.

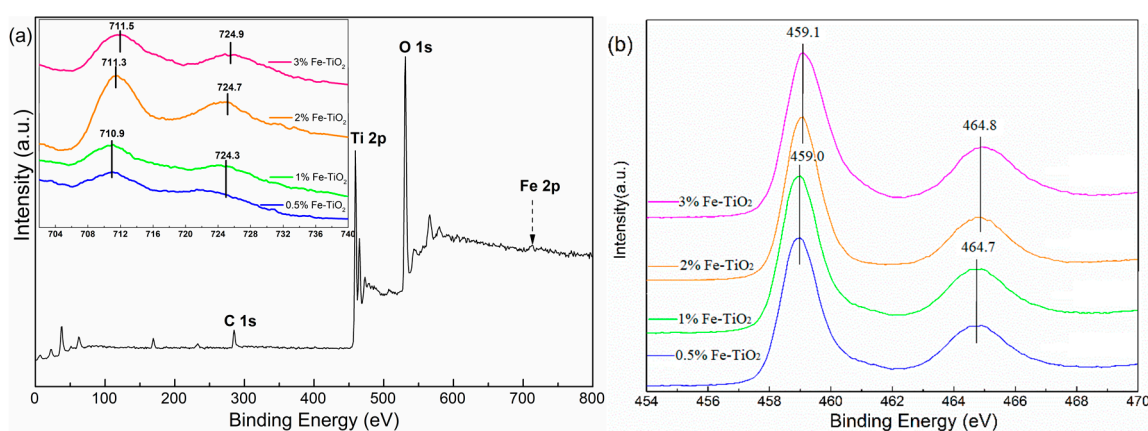


Figure 7. XPS spectra of 2% Fe-doped TiO₂ samples (a) The Fe 2p_{1/2}, Fe 2p_{3/2}, Ti 2p_{1/2}, and Ti 2p_{3/2} spectra for the 0.5%, 1%, 2%, and 3% Fe-doped TiO₂ samples, respectively, are given in inset (a) and (b).

To further investigate the lattice site occupancy around the iron ion in the TiO₂ host, electron paramagnetic resonance (EPR) experiments of the iron-loaded TiO₂ samples were conducted and the results are presented in Figure 8. The EPR signals observed at $g = 1.99$ and $g = 4.22$ were attributed to Fe³⁺ substituted for Ti⁴⁺ in the matrix of TiO₂ and to the substitutional incorporation of isolated iron cations dispersed on the TiO₂ surface, respectively [27,36,37]. According to the standard Kroger–Vink equation, the acceptor-type Fe³⁺ dopant in the TiO₂ lattice could act as defective sites ($V_{\text{O}}^{\bullet\bullet} - \text{Fe}'_{\text{Ti}}$) and generate oxygen vacancies ($V_{\text{O}}^{\bullet\bullet}$) [38,39].



Meanwhile, a comparison of the spectral characteristics among the tested samples showed that the $g = 4.22$ resonance band increases with the iron content compared with the signal at $g = 1.99$, indicating that more doped iron cations were located on the TiO₂ surface.

To investigate the reducibility behaviour of the bare and Fe-supported TiO₂, a series of H₂-TPR experiments were conducted and the results are shown in Figure 9. It can be seen that, in the pure TiO₂ sample, a broad signal was presented ranging from 500 °C to 650 °C, and the two reduction peaks located at 585 °C and 613 °C can be ascribed to the surface oxygen and lattice oxygen due to Ti⁴⁺ to Ti³⁺ [40]. When Fe was incorporated into the TiO₂ support, a distinct overlapped peak shifted to the lower temperature range (400–565 °C). Meanwhile, the peak intensity showed a significant increase as the Fe-doped concentration increased from 0.5% to 2%, and weak growth could be observed with a further increase in Fe-doped concentration. These results indicate that the integration of Fe

with the TiO_2 nanoparticle could enhance the oxidative ability of the TiO_2 . To better understand the detailed reduction properties of Fe species, a peak-fitting process was performed according to the method proposed by Liu et al. [41]. As shown in Figure 9, all of the Fe-doped TiO_2 reduction peaks can be divided into four sub-bands and denominated as T_1 , T_2 , T_3 , and T_4 . The sub-band T_1 and sub-bands T_2 – T_4 are assigned to the surface oxygen and lattice oxygen, respectively [42]. Specially, the T_2 , T_3 , and T_4 bands correspond to the progressive reduction process of the Fe ion, i.e., $\text{Fe}^{3+}\text{-O-Ti} \rightarrow \text{Fe}^{2+/3+}\text{-O-Ti} \rightarrow \text{Fe}^{2+}\text{-O-Ti} \rightarrow \text{Fe}^0$ [43]. The area ratio values of $T_1/(T_2 + T_3)$ were all below 1:2, indicating that the $\text{Fe}^{3+}\text{-O-Ti}$ has been really converted into Fe^0 in the T_3 – T_4 process. It is worth mentioning that the area ratio values of $T_1/(T_2 + T_3)$ decreased with an increase in Fe-doped concentration, and this phenomenon should be attributed to the fact that an increase in Fe-doped concentration facilitates the enrichment of isolated Fe^{3+} on the surface of TiO_2 (hereafter denoted as $\text{Fe}^{3+}_{\text{surface}}$). The results are consistent with the above EPR analysis.

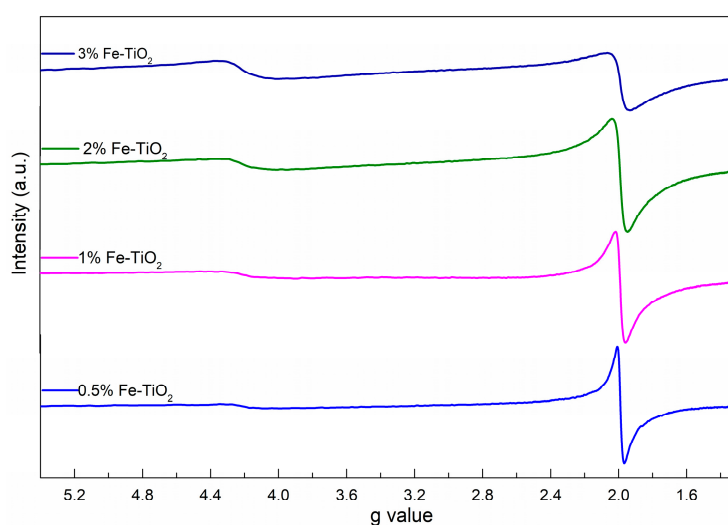


Figure 8. Electron paramagnetic resonance (EPR) spectra of Fe-doped TiO_2 samples.

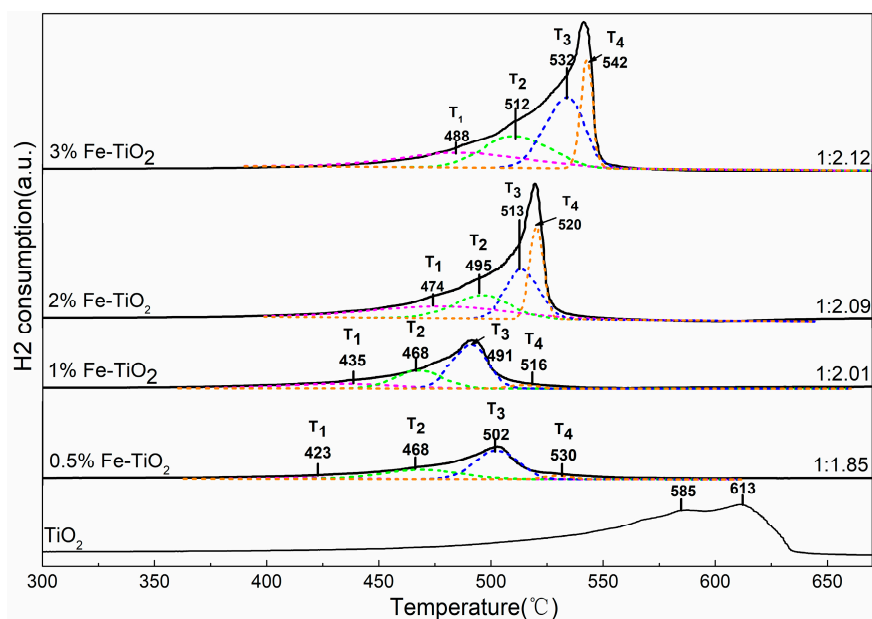


Figure 9. H_2 -TPR profiles of the pure and Fe-doped TiO_2 samples.

As proposed above, $\bullet\text{OH}$ served as putative contributors to the removal of NO , where P25 and the as-prepared materials were used as catalysts to decompose H_2O_2 . As shown in Figure 10, the observed hyperfine splitting constants for the 1:2:2:1 signal ($a\text{N} = a\text{H} = 14.9\text{ G}$) were the typical spectrum shape of the DMPO-OH spin adduct and were in good accordance with the values in the literature [44]. What is more, the concentration of $\bullet\text{OH}$ was in the order of: $2\% \text{ Fe-TiO}_2 + \text{H}_2\text{O}_2 > \text{TiO}_2 + \text{H}_2\text{O}_2 > \text{P25} + \text{H}_2\text{O}_2 > \text{H}_2\text{O}_2$. This order was identical to the NO_x removal efficiency and evidenced that the as-prepared catalysts facilitated the production of $\bullet\text{OH}$.

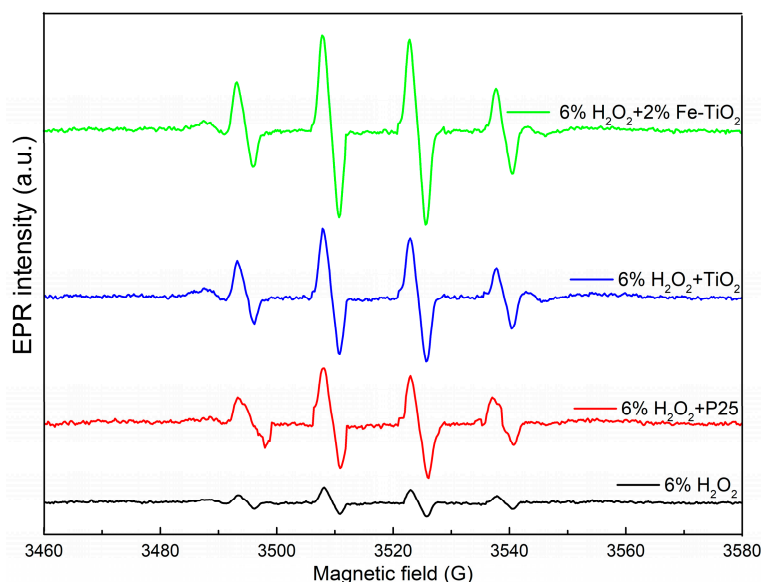


Figure 10. EPR spectra of radical adducts with DMPO in H_2O_2 , $\text{H}_2\text{O}_2 + \text{P25}$, $\text{H}_2\text{O}_2 + \text{TiO}_2$, and $\text{H}_2\text{O}_2 + 2\% \text{ Fe/TiO}_2$ systems.

2.5. Mechanistic Discussion

To elucidate in depth the functional mechanism and promotional effect of Fe species on the oxidative activity of NO_x , a fixed Fe/Ti molar ratio of 2% treated at different calcination temperatures were selected to test the catalytic activities. As shown in Figure 11a–d, the sample treated at $450\text{ }^\circ\text{C}$ yielded the highest NO_x removal efficiency of 95.67% and the conversion efficiency of NO to HNO_3 was 88.1%. The XRD patterns of the Fe/ TiO_2 samples (Figure S4) revealed that samples treated at $T_{\text{anneal}} \leq 400\text{ }^\circ\text{C}$ exhibited a hybrid crystalline feature of the amorphous gel and a small grain size anatase structure, while the samples annealing at temperatures ranging from $400\text{ }^\circ\text{C}$ to $600\text{ }^\circ\text{C}$ all exhibited a pure anatase phase [45]. Moreover, a trace amount of the characteristic peaks of $\alpha\text{-Fe}_2\text{O}_3$ ($2\theta = 32.4^\circ$ and 34.6°) was detected in the samples annealed below $400\text{ }^\circ\text{C}$ and disappeared as the calcination temperature increased. The XPS results (Figure S5a) suggested that the iron species in the samples treated below $400\text{ }^\circ\text{C}$ were assigned to Fe_2O_3 , further confirming the existence of phase segregation and verifying that a low annealing temperature is unfavorable for Fe^{3+} substituting for Ti^{4+} in the TiO_2 matrix [46]. In comparison, the peaks of Fe 2p_{3/2} and Fe 2p_{1/2} of the samples treated at temperatures ranging from $400\text{ }^\circ\text{C}$ to $500\text{ }^\circ\text{C}$ shift higher, and this phenomenon could account for the cooperative formation of positively charged surface Fe^{3+} and Fe^{3+} in the Ti-O-Fe species [47,48]. Interestingly, the Fe 2p level binding energy exhibited a negative shift when the calcination temperature was over $500\text{ }^\circ\text{C}$, and the peak positions corresponded with the characteristics of a pure Ti-O-Fe species. The appearance of two distinct peaks of Ti 2p_{1/2} ($464.4\text{--}464.7\text{ eV}$) and Ti 2p_{3/2} ($458.7\text{--}458.8\text{ eV}$) confirmed that all Ti ions were in the +4 valence state (Figure S5b). The EPR spectra of the samples gave direct evidence that an elevated temperature treatment facilitated the iron ions diffusing from the surface into the bulk of TiO_2 (Figure S6).

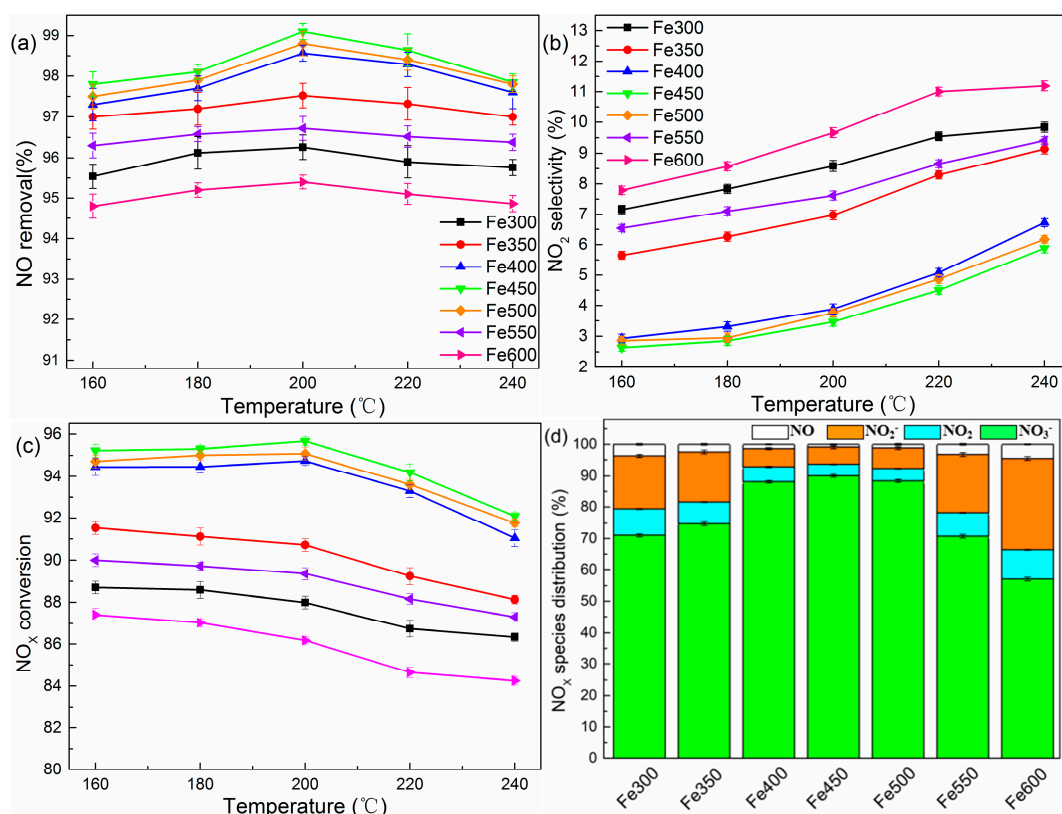


Figure 11. (a–d) Removal efficiencies of NO_x over Fe/TiO₂ treated at different calcination temperatures. Conditions: H₂O₂/NO molar ratio: 12:1; GHSV: 60,000 h^{−1}.

Based on the above analysis, the promotion effect of iron species on the catalytic activity could be represented in the following two respects. On one hand, a certain proportion of Fe³⁺ in the matrix of TiO₂ ($g = 1.99$, hereafter denoted as Fe³⁺_{matrix}) generated the positively charged oxygen vacancies by compensating for the negative charge acceptor dopant [38]. The oxygen vacancies site acted as a catalytic center and facilitated the formation of •OH by the catalytic decomposition of H₂O₂ vapor. The highly oxidative radical groups contributed to the charge separation process as well as the oxidation of NO. On the other hand, a minor fraction of Fe³⁺ on the TiO₂ surface showed a remarkable inhibition of NO₂; similar results were reported by Wu et al. [38]. Specifically, some Fe³⁺ sites would be reduced into Fe²⁺ during the redox process of an H₂O₂ molecule, while Fe²⁺, which holds a strong affinity for NO, could easily adsorb the NO molecules and form a Fe²⁺(NO)_x polynitrosyl species [49,50]. Then, this species could be oxidized via the adjacent •OH. As a result, the introduction of appropriate Fe³⁺_{surface} and Fe³⁺_{matrix} were responsible for the superior performance of the Fe-TiO₂ catalyst.

3. Materials and Methods

3.1. Experimental Apparatus and Procedure

The experiments were carried out in a fixed-bed system as presented in Figure 12. The system consisted of four sections: a simulated flue gas generating section, a quartz-made integrated reactor for hydrogen peroxide vaporization and NO oxidation, an absorption section, and a flue gas analyser. N₂ and NO (1% (v/v), balanced with N₂) compressed gas cylinders (Dalian Special Gases Co., Ltd., Dalian, China) were used to generate simulated flue gas. The total gas flow which passed through the catalyst was fixed at 1 L/min controlled by mass flow meter (MCF), wherein the NO_x content was 500 ppm. Some 0.3 mL/min 3 wt %, 6 wt %, 9 wt %, and 12 wt % H₂O₂ solution (30.0%, Sinopharm

Chemical Reagent, Shanghai, China), which corresponded to a molar $\text{H}_2\text{O}_2/\text{NO}$ of 8, 12, 24, and 48, respectively, was pumped by a peristaltic pump (Longer Precision Pump Co., Ltd., Baoding, China), carried by 200 mL/min N_2 , and vaporized through a heating apparatus (140°C). The gas mixture was injected into the catalyst zone with the simulated flue gas. The H_2O_2 vapor decomposed to produce the oxidative free radicals via a typical surface catalysis reaction. As the catalytic decomposition process of the H_2O_2 vapor occurred in the stream of simulated flue gas, the oxidative free radicals rapidly converted NO into HNO_2 , NO_2 , and HNO_3 . Two scrubbers, made of a gas-washing bottle filled with NaOH solution (0.2 mol/L, 0.3 L), were utilized to remove the HNO_2 and HNO_3 in the mist. As demonstrated by Wang et al., up to 83% NO_2 would not be absorbed by NaOH solution, which then remained in the exhaust gas [51–53]. Therefore, the NO and NO_2 remaining in the gas measured by a flue gas analyser (Madur Photon PGD-100, Madurai Eljack Electronics Co., Vienna, Austria) can represent the real NO_x removal efficiency. The NO_2^- and NO_3^- ions in the sample solutions were determined by ion chromatography (Dionex 4000, Dionex Corp., Sunnyvale, CA, USA). The chromatographic conditions were: AS14 anion column, eluent solution (3.5 mM Na_2CO_3 /1.0 mM NaHCO_3), flowrate (1.2 mL/min), column temperature (25°C). The qualitative results of the ion products in the scrubber solution were analyzed via the retention time and the peak area, respectively.

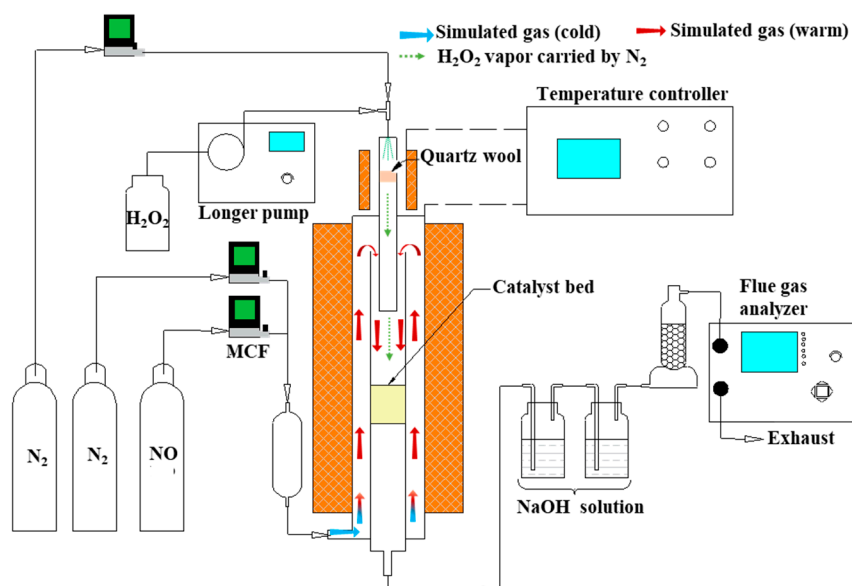


Figure 12. Schematic diagram of the experimental setup.

3.2. Catalyst Preparation

Nanosize TiO_2 (P25) was purchased from Evonik Industries AG (Essen, Germany). The catalyst was heated at 400°C for 6 h in air to remove impurities. The Fe/ TiO_2 catalysts were prepared by the co-precipitation method, and the details of the process can be found in [28,54,55]. A calculated amount of $\text{Fe}(\text{NO}_3)_3 \cdot 9\text{H}_2\text{O}$ (98.5%, Sinopharm Chemical Reagent, Shanghai, China) and $\text{Ti}(\text{SO}_4)_2$ (97%, Sinopharm Chemical Reagent, Shanghai, China) (the molar ratios of Fe/Ti were 0.5%, 1%, 2%, and 3%, respectively) were dissolved in ice-cold deionized water and stirred for 1 h, then standard ammonia solution (25%, Sinopharm Chemical Reagent, Shanghai, China) was added slowly to the solution under stirring until the pH rose to 10. Without aging, the obtained precipitate was filtered and washed by deionized water. The resulting powder was desiccated at 105°C for 12 h and then calcined in air at 400°C for 6 h. All samples were ground and sieved to 60–80 mesh for activity tests. The catalysts prepared by the co-precipitation procedure were labelled as TiO_2 , 0.5% Fe- TiO_2 , 1% Fe- TiO_2 , 2% Fe- TiO_2 , and 3% Fe- TiO_2 in order based on the loading concentration of the iron element, whereas the TiO_2 (P25) was named P25.

3.3. Catalyst Characterization

Visible-Raman spectra of the catalysts were collected on a UV resonance Raman spectrometer (LabRAM HR800, Horiba JobinYvon, Bensheim, Germany) using a 532 nm laser. The textural properties of the samples were specified using liquid nitrogen adsorption at $-196\text{ }^{\circ}\text{C}$ in a physisorption analyzer (Micromeritics ASAP 2020M, Micromeritics Instrument Corp., Norcross, GA, USA). The specific surface area was calculated by the Brunauer–Emmett–Teller (BET) method. The crystalline phase of the sample was identified by Powder X-ray Diffraction (XRD, PANalytical B.V., Almelo, The Netherlands) with a high-intensity Cu K α radiation source ($\lambda = 1.5406\text{ \AA}$). The XRD pattern was collected over a range of 2θ angles from 10° to 90° at a step size of $8^{\circ}\text{ min}^{-1}$. The average crystallite size of the sample was estimated using Debye–Scherrer’s equation (Equation (1)), where the shape factor K is a constant taken as 0.89, β is the full width at half maximum (FWHM) of the diffraction peak, θ is the Bragg angle, and λ is the X-ray wavelength that corresponds to Cu K α radiation ($\lambda = 1.5406\text{ \AA}$).

$$D = \frac{K\lambda}{\beta \cos \theta} \quad (9)$$

Field emission scanning electron microscopy (SEM, Hitachi SU-8010, Hitachi High Technologies Co., Hitachi, Japan) and transmission electron microscopy (TEM, FEI G2F30, FEI Co., Hillsboro, OR, USA) were used to identify the surface morphology of the samples. XPS measurements were recorded using a Thermo Scientific ESCALAB 250XI photoelectron spectrometer with Al K α ($h\nu = 1486.6\text{ eV}$, Thermo Fisher Scientific Inc., Waltham, MA, USA) X-ray radiation. Additionally, the shift of the binding energy was corrected using the C1s level at 284.8 eV as an internal standard. The X-band (9.4 GHz) electron paramagnetic resonance (EPR) spectrum was collected on a Bruker EPR spectrometer (A300-9.5/12, Bruker Instruments, Karlsruhe, Germany) at room temperature. Temperature programmed reduction (TPR) measurements were carried out on a CHEMBET 3000 instrument (Quantachrome Instruments, Boynton Beach, FL, USA). Prior to the TPR experiments, a 100 mg sample was purged with helium gas for 15 min. Then, the sample was preheated to $300\text{ }^{\circ}\text{C}$ and left for 30 min. After it cooled to ambient temperature, the catalyst was reduced in a flow rate of 10% H_2/Ar (30 mL/min) and a linear heating rate of $5\text{ }^{\circ}\text{C}/\text{min}$ to $670\text{ }^{\circ}\text{C}$. $\bullet\text{OH}$ was captured by 5,5-dimethyl-1-pyrroline N-oxide (DMPO, 97%, Sigma-Aldrich, St. Louis, MO, USA) and detected by ESR spectrometer. The details of the process can be found in Wiedmer and Sánchez [44,56]. Specially, the operating conditions were set as follows: modulation frequency (100 kHz), modulation amplitude (4 G), resonance frequency (9.87 GHz), sweep width (200 G), microwave power (19.22 mW), centre field (3522 G).

3.4. Data Process

The deNO_x performance can be assessed separately for NO oxidation, NO_2 selectivity, and NO_x removal ($\text{NO}_x = \text{NO} + \text{NO}_2$) by using Equations (2)–(4) [28]. The values used were the average of those collected after 2 h at a steady state, and the tests were repeated three times to ensure their reproducibility. Meanwhile, the overall nitrogen mass balance was calculated in order to elucidate the catalytic oxidation ability of the catalysts.

$$\text{NO removal} = \frac{\text{NO}_{in} - \text{NO}_{out}}{\text{NO}_{in}} \quad (10)$$

$$\text{NO}_2 \text{ selectivity} = \frac{\text{NO}_{2,out}}{\text{NO}_{in} - \text{NO}_{out}} \quad (11)$$

$$\text{NO}_x \text{ conversion} = \frac{\text{NO}_{x,in} - \text{NO}_{x,out}}{\text{NO}_{x,in}} \quad (12)$$

4. Conclusions

A novel denitrification process with H_2O_2 vapor catalyzed by a TiO_2 -based catalyst was proposed. Meanwhile, a series of Fe-doped anatase TiO_2 nanoparticles were prepared with the aim of complementing the developed system. Notably, the Fe/ TiO_2 exhibited remarkably high activity with a high utilization efficiency of H_2O_2 . A detailed study was carried out on the Fe/ TiO_2 catalyst. The highest NO_x removal efficiency achieved was 95.6%, and a molar $\text{NO}_3^-/\text{NO}_2^-$ of 16.2 was also achieved. The catalyst characterization results demonstrated that the strong enhancement of the deep oxidation efficiency was evidenced to be related to the NO absorptivity of iron ions on the TiO_2 surface and O vacancies caused by the $\text{Fe}^{3+}_{\text{matrix}}$.

Supplementary Materials: The following are available online at www.mdpi.com/2073-4344/7/12/386/s1, Figure S1. Removal efficiencies of NO_x in blank tests; Figure S2. N_2 adsorption/desorption isotherms of the samples. (a) P25, (b) TiO_2 , (c) 0.5% Fe- TiO_2 , (d) 1% Fe- TiO_2 , (e) 2% Fe- TiO_2 , and (f) 3% Fe- TiO_2 ; Figure S3. FE-SEM images of the catalyst samples. (a) P25, (b) TiO_2 , (c) 0.5% Fe- TiO_2 , (d) 1% Fe- TiO_2 , (e) 2% Fe- TiO_2 , and (f) 3% Fe- TiO_2 ; Figure S4. X-ray powder diffraction patterns of the samples calcined at different temperatures; Figure S5. X-ray photoelectron spectra for the samples calcined at different temperatures; Figure S6. EPR Spectra of the iron-loaded samples at different heating temperatures.

Acknowledgments: The authors appreciate greatly the financial support from the Research Fund for the “Fundamental Research Funds for the Central Universities” and the technical support from the Analytical and Testing Center in Huazhong University of Science & Technology (<http://atc.hust.edu.cn>). We appreciate deeply the help of Jinping Zhang, Jiajia Cui, and Penghui Guo for assistance and thank Maochang Liu, Haiping Yang, and Xianhua Wang for helpful suggestions of the manuscript.

Author Contributions: Lei Chen, Yuxin Li, Qiang Lu, and Qinxin Zhao conceived and designed the experiments; Lei Chen performed the experiments; Lei Chen, Qiang Lu, and Zhiyuan Liang analyzed the data; Lei Chen, Qiang Lu, and Yungang Wang contributed reagents/materials/analysis tools; and Lei Chen, Qiang Lu, and Qinxin Zhao wrote the paper.

Conflicts of Interest: The authors declare no conflict of interest.

References

- Skalska, K.; Miller, J.S.; Ledakowicz, S. Trends in NO_x abatement: A review. *Sci. Total Environ.* **2010**, *408*, 3976–3989. [CrossRef] [PubMed]
- Marberger, A.; Elsener, M.; Ferri, D.; Kröcher, O. VO_x surface coverage optimization of $\text{V}_2\text{O}_5/\text{WO}_3\text{-TiO}_2$ SCR catalysts by variation of the v loading and by aging. *Catalysts* **2015**, *5*, 1704–1720. [CrossRef]
- Dong, L.; Fan, Y.; Ling, W.; Yang, C.; Huang, B. Effect of Ce/ γ Addition on Low-Temperature SCR Activity and SO_2 and H_2O Resistance of $\text{MnO}_x/\text{ZrO}_2/\text{MWCNTs}$ Catalysts. *Catalysts* **2017**, *7*, 181. [CrossRef]
- Liu, Y.; Wang, Q.; Yin, Y.; Pan, J.; Zhang, J. Advanced oxidation removal of NO and SO_2 from flue gas by using ultraviolet/ H_2O_2 /NaOH process. *Chem. Eng. Res. Des.* **2014**, *92*, 1907–1914. [CrossRef]
- Liu, Y.; Zhang, J.; Sheng, C.; Zhang, Y.; Zhao, L. Preliminary study on a new technique for wet removal of nitric oxide from simulated flue gas with an ultraviolet (UV)/ H_2O_2 process. *Energy Fuels* **2010**, *24*, 4925–4930. [CrossRef]
- Ding, J.; Zhong, Q.; Zhang, S. Catalytic efficiency of iron oxides in decomposition of H_2O_2 for simultaneous NO_x and SO_2 removal: Effect of calcination temperature. *J. Mol. Catal. A Chem.* **2014**, *393*, 222–231. [CrossRef]
- Ding, J.; Zhong, Q.; Zhang, S.; Cai, W. Size-and shape-controlled synthesis and catalytic performance of iron–aluminum mixed oxide nanoparticles for NO_x and SO_2 removal with hydrogen peroxide. *J. Hazard. Mater.* **2015**, *283*, 633–642. [CrossRef] [PubMed]
- Ding, J.; Zhong, Q.; Zhang, S.; Song, F.; Bu, Y. Simultaneous removal of NO_x and SO_2 from coal-fired flue gas by catalytic oxidation-removal process with H_2O_2 . *Chem. Eng. J.* **2014**, *243*, 176–182. [CrossRef]
- Zhao, Y.; Yuan, B.; Hao, R.; Tao, Z. Low-temperature conversion of no in flue gas by vaporized H_2O_2 and nanoscale zerovalent iron. *Energy Fuels* **2017**, *31*, 7282–7289. [CrossRef]
- Wu, B.; Xiong, Y.; Ge, Y. Simultaneous removal of SO_2 and NO from flue gas with $\cdot\text{OH}$ from the catalytic decomposition of gas-phase H_2O_2 over solid-phase $\text{Fe}_2(\text{SO}_4)_3$. *Chem. Eng. J.* **2017**. [CrossRef]
- Wu, B.; Xiong, Y. A novel low-temperature no removal approach with $\cdot\text{OH}$ from catalytic decomposition of H_2O_2 over $\text{La}_{1-x}\text{Ca}_x\text{FeO}_3$ oxides. *J. Chem. Technol. Biotechnol.* **2017**. [CrossRef]

12. Gupta, S.M.; Tripathi, M. A review of TiO₂ nanoparticles. *Chin. Sci. Bull.* **2011**, *56*, 1639. [[CrossRef](#)]
13. Lousada, C.M.; Yang, M.; Nilsson, K.; Jonsson, M. Catalytic decomposition of hydrogen peroxide on transition metal and lanthanide oxides. *J. Mol. Catal. A Chem.* **2013**, *379*, 178–184. [[CrossRef](#)]
14. Lousada, C.M.; LaVerne, J.A.; Jonsson, M. Enhanced hydrogen formation during the catalytic decomposition of H₂O₂ on metal oxide surfaces in the presence of HO radical scavengers. *Phys. Chem. Chem. Phys.* **2013**, *15*, 12674–12679. [[CrossRef](#)] [[PubMed](#)]
15. Suh, M.; Bagus, P.S.; Pak, S.; Rosynek, M.P.; Lunsford, J.H. Reactions of hydroxyl radicals on titania, silica, alumina, and gold surfaces. *J. Phys. Chem. B* **2000**, *104*, 2736–2742. [[CrossRef](#)]
16. Li, L.; Shen, Q.; Cheng, J.; Hao, Z. Catalytic oxidation of NO over TiO₂ supported platinum clusters. II: Mechanism study by in situ FTIR spectra. *Catal. Today* **2010**, *158*, 361–369. [[CrossRef](#)]
17. Ding, J.; Lin, J.; Xiao, J.; Zhang, Y.; Zhong, Q.; Zhang, S.; Guo, L.; Fan, M. Effect of fluoride doping for catalytic ozonation of low-temperature denitrification over cerium–titanium catalysts. *J. Alloys Compd.* **2016**, *665*, 411–417. [[CrossRef](#)]
18. Liu, Y.; Zhang, J.; Pan, J.; Tang, A. Investigation on the removal of NO from SO₂-containing simulated flue gas by an ultraviolet/Fenton-like reaction. *Energy Fuels* **2012**, *26*, 5430–5436. [[CrossRef](#)]
19. Hao, R.; Zhao, Y.; Yuan, B.; Zhou, S.; Yang, S. Establishment of a novel advanced oxidation process for economical and effective removal of SO₂ and NO. *J. Hazard. Mater.* **2016**, *318*, 224–232. [[CrossRef](#)] [[PubMed](#)]
20. Liu, Y.X.; Zhang, J. Photochemical oxidation removal of NO and SO₂ from simulated flue gas of coal-fired power plants by wet scrubbing using UV/H₂O₂ advanced oxidation process. *Ind. Eng. Chem. Res.* **2011**, *50*, 3836–3841. [[CrossRef](#)]
21. Li, X.; Chen, C.; Zhao, J. Mechanism of photodecomposition of H₂O₂ on TiO₂ surfaces under visible light irradiation. *Langmuir* **2001**, *17*, 4118–4122. [[CrossRef](#)]
22. Setiabudi, A.; Chen, J.; Mul, G.; Makkee, M.; Moulijn, J.A. CeO₂ catalysed soot oxidation: The role of active oxygen to accelerate the oxidation conversion. *Appl. Catal. B Environ.* **2004**, *51*, 9–19. [[CrossRef](#)]
23. Sivachandiran, L.; Thevenet, F.; Gravejat, P.; Rousseau, A. Investigation of NO and NO₂ adsorption mechanisms on TiO₂ at room temperature. *Appl. Catal. B Environ.* **2013**, *142*, 196–204. [[CrossRef](#)]
24. Mikami, M.; Nakamura, S.; Kitao, O.; Arakawa, H. Lattice dynamics and dielectric properties of TiO₂ anatase: A first-principles study. *Phys. Rev. B* **2002**, *66*, 155213. [[CrossRef](#)]
25. Ganesh, I.; Kumar, P.P.; Gupta, A.K.; Sekhar, P.S.; Radha, K.; Padmanabham, G.; Sundararajan, G. Preparation and characterization of Fe-doped TiO₂ powders for solar light response and photocatalytic applications. *Proc. Appl. Ceram.* **2012**, *6*, 21–36. [[CrossRef](#)]
26. Zhang, G.K.; Ding, X.M.; He, F.S.; Yu, X.Y.; Zhou, J.; Hu, Y.J.; Xie, J.W. Low-temperature synthesis and photocatalytic activity of TiO₂ pillared montmorillonite. *Langmuir* **2008**, *24*, 1026–1030. [[CrossRef](#)] [[PubMed](#)]
27. Tong, T.; Zhang, J.; Tian, B.; Chen, F.; He, D. Preparation of Fe³⁺-doped TiO₂ catalysts by controlled hydrolysis of titanium alkoxide and study on their photocatalytic activity for methyl orange degradation. *J. Hazard. Mater.* **2008**, *155*, 572–579. [[CrossRef](#)] [[PubMed](#)]
28. Wang, C.; Böttcher, C.; Bahnemann, D.W.; Dohrmann, J.K. A comparative study of nanometer sized Fe(III)-doped TiO₂ photocatalysts: Synthesis, characterization and activity. *J. Mater. Chem.* **2003**, *13*, 2322–2329. [[CrossRef](#)]
29. Adán, C.; Bahamonde, A.; Fernández-García, M.; Martínez-Arias, A. Structure and activity of nanosized iron-doped anatase TiO₂ catalysts for phenol photocatalytic degradation. *Appl. Catal. B Environ.* **2007**, *72*, 11–17. [[CrossRef](#)]
30. Asiltürk, M.; Sayilkan, F.; Arpaç, E. Effect of Fe³⁺ ion doping to TiO₂ on the photocatalytic degradation of malachite green dye under UV and vis-irradiation. *J. Photochem. Photobiol.* **2009**, *203*, 64–71. [[CrossRef](#)]
31. Shannon, R.T. Revised effective ionic radii and systematic studies of interatomic distances in halides and chalcogenides. *Acta Crystallogr. Sect. A* **1976**, *32*, 751–767. [[CrossRef](#)]
32. Alqurashi, G.K.; Al-Shehri, A.; Narasimharao, K. Effect of TiO₂ morphology on the benzyl alcohol oxidation activity of Fe₂O₃–TiO₂ nanomaterials. *RSC Adv.* **2016**, *6*, 71076–71091. [[CrossRef](#)]
33. Wu, Q.; Zheng, Q.; van de Krol, R. Creating oxygen vacancies as a novel strategy to form tetrahedrally coordinated Ti⁴⁺ in Fe/TiO₂ nanoparticles. *J. Phys. Chem. C* **2012**, *116*, 7219–7226. [[CrossRef](#)]

34. Kayhan, E.; Andonova, S.M.; Şentürk, G.S.; Chusuei, C.C.; Ozensoy, E. Fe promoted NO_x storage materials: Structural properties and NO_x uptake. *J. Phys. Chem. C* **2010**, *114*, 357–369. [[CrossRef](#)]
35. Xiao, L.; Zhang, J.; Cong, Y.; Tian, B.; Chen, F.; Anpo, M. Synergistic effects of doped Fe³⁺ and deposited Au on improving the photocatalytic activity of TiO₂. *Catal. Lett.* **2006**, *111*, 207–211. [[CrossRef](#)]
36. Niu, Y.; Xing, M.; Zhang, J.; Tian, B. Visible light activated sulfur and iron co-doped TiO₂ photocatalyst for the photocatalytic degradation of phenol. *Catal. Today* **2013**, *201*, 159–166. [[CrossRef](#)]
37. Wu, Q.; van de Krol, R. Selective photoreduction of nitric oxide to nitrogen by nanostructured TiO₂ photocatalysts: Role of oxygen vacancies and iron dopant. *J. Am. Chem. Soc.* **2012**, *134*, 9369–9375. [[CrossRef](#)] [[PubMed](#)]
38. Chiang, Y.-M.; Birnie, D.P.; Kingery, W.D. *Physical Ceramics: Principles for Ceramic Science and Engineering*; John Wiley & Sons, Inc.: Hoboken, NJ, USA, 1997.
39. Ding, J.; Zhong, Q.; Cai, H.; Zhang, S. Structural characterizations of fluoride doped ceti nanoparticles and its differently promotional mechanisms on ozonation for low-temperature removal of NO_x (x = 1, 2). *Chem. Eng. J.* **2016**, *286*, 549–559. [[CrossRef](#)]
40. Liu, F.; He, H. Selective catalytic reduction of NO with NH₃ over manganese substituted iron titanate catalyst: Reaction mechanism and H₂O/SO₂ inhibition mechanism study. *Catal. Today* **2010**, *153*, 70–76. [[CrossRef](#)]
41. Liu, F.; He, H. Structure-activity relationship of iron titanate catalysts in the selective catalytic reduction of NO_x with NH₃. *J. Phys. Chem. C* **2010**, *114*, 16929–16936. [[CrossRef](#)]
42. Liu, F.; He, H.; Ding, Y.; Zhang, C. Effect of manganese substitution on the structure and activity of iron titanate catalyst for the selective catalytic reduction of NO with NH₃. *Appl. Catal. B Environ.* **2009**, *93*, 194–204. [[CrossRef](#)]
43. Hung, W.C.; Chen, Y.C.; Chu, H.; Tseng, T.K. Synthesis and characterization of TiO₂ and Fe/TiO₂ nanoparticles and their performance for photocatalytic degradation of 1,2-dichloroethane. *Appl. Surf. Sci.* **2008**, *255*, 2205–2213. [[CrossRef](#)]
44. Farhangi, N.; Ayissi, S.; Charpentier, P.A. Fe doped TiO₂–graphene nanostructures: Synthesis, DFT modeling and photocatalysis. *Nanotechnology* **2014**, *25*, 305601. [[CrossRef](#)] [[PubMed](#)]
45. Wang, C.C.; Wang, K.W.; Perng, T.P. Electron field emission from Fe-doped TiO₂ nanotubes. *Appl. Phys. Lett.* **2010**, *96*, 143102. [[CrossRef](#)]
46. Zhang, J.; Chen, X.; Shen, Y.; Li, Y.; Hu, Z.; Chu, J. Synthesis, surface morphology, and photoluminescence properties of anatase iron-doped titanium dioxide nano-crystalline films. *Phys. Chem. Chem. Phys.* **2011**, *13*, 13096–13105. [[CrossRef](#)] [[PubMed](#)]
47. Mihaylov, M.; Ivanova, E.; Drenchev, N.; Hadjiivanov, K. Coordination Chemistry of Fe²⁺ Ions in Fe, H-ZSM-5 Zeolite as Revealed by the IR Spectra of Adsorbed CO and NO. *J. Phys. Chem. C* **2010**, *114*, 1004–1014. [[CrossRef](#)]
48. Ivanova, E.; Mihaylov, M.; Hadjiivanov, K.; Blasin-Aubé, V.; Marie, O.; Plesniar, A.; Daturi, M. Evidencing three distinct Fe II sites in Fe–FER zeolites by using CO and NO as complementary IR probes. *Appl. Catal. B Environ.* **2010**, *93*, 325–338. [[CrossRef](#)]
49. Wang, Z.; Cen, K.; Zhou, J.; Fan, J. *Simultaneous Multi-Pollutants Removal in Flue Gas by Ozone*; Springer: Berlin/Heidelberg, Germany, 2014.
50. Thomas, D.; Vanderschuren, J. Nitrogen oxides scrubbing with alkaline solutions. *Chem. Eng. Technol.* **2000**, *23*, 449–455. [[CrossRef](#)]
51. Kameoka, Y.; Pigford, R.L. Absorption of nitrogen dioxide into water, sulfuric acid, sodium hydroxide, and alkaline sodium sulfite aqueous solutions. *Ind. Eng. Chem. Fundam.* **1977**, *16*, 163–169. [[CrossRef](#)]
52. Liu, F.; He, H.; Zhang, C. Novel iron titanate catalyst for the selective catalytic reduction of NO with NH₃ in the medium temperature range. *Chem. Commun.* **2008**, *17*, 2043–2045. [[CrossRef](#)] [[PubMed](#)]
53. Liu, F.; Asakura, K.; He, H.; Shan, W.; Shi, X.; Zhang, C. Influence of sulfation on iron titanate catalyst for the selective catalytic reduction of NO_x with NH₃. *Appl. Catal. B Environ.* **2011**, *103*, 369–377. [[CrossRef](#)]
54. Ma, J.; He, H.; Liu, F. Effect of Fe on the photocatalytic removal of NO_x over visible light responsive Fe/TiO₂ catalysts. *Appl. Catal. B Environ.* **2015**, *179*, 21–28. [[CrossRef](#)]

55. Wiedmer, D.; Sagstuen, E.; Welch, K.; Haugen, H.J.; Tiainen, H. Oxidative power of aqueous non-irradiated $\text{TiO}_2\text{-H}_2\text{O}_2$ suspensions: Methylene blue degradation and the role of reactive oxygen species. *Appl. Catal. B Environ.* **2016**, *198*, 9–15. [[CrossRef](#)]
56. Sánchez, L.D.; Taxt-Lamolle, S.F.M.; Hole, E.O.; Krivokapić, A.; Sagstuen, E.; Haugen, H.J. TiO_2 suspension exposed to H_2O_2 in ambient light or darkness: Degradation of methylene blue and EPR evidence for radical oxygen species. *Appl. Catal. B Environ.* **2013**, *142*, 662–667. [[CrossRef](#)]



© 2017 by the authors. Licensee MDPI, Basel, Switzerland. This article is an open access article distributed under the terms and conditions of the Creative Commons Attribution (CC BY) license (<http://creativecommons.org/licenses/by/4.0/>).